AIAA 2003-3875

OPTIMUM SHAPE DESIGN FOR UNSTEADY FLOWS USING TIME ACCURATE AND NON-LINEAR FREQUENCY DOMAIN METHODS

Siva K. Nadarajah
Department of Mechanical Engineering
McGill University
Montreal, QC H3A 2S6 Canada

Matthew S. McMullen and Antony Jameson
Department of Aeronautics and Astronautics
Stanford University
Stanford, California 94305 U.S.A.

16th AIAA Computational Fluid Dynamics Conference
June 23–26, 2003, Orlando, Florida

AIAA 2003-3875

OPTIMUM SHAPE DESIGN FOR UNSTEADY FLOWS USING TIME ACCURATE AND NON-LINEAR FREQUENCY DOMAIN METHODS

Siva K. Nadarajah *
Department of Mechanical Engineering
McGill University
Montreal, QC H3A 2S6 Canada

Matthew S. McMullen† and Antony Jameson ‡
Department of Aeronautics and Astronautics
Stanford University
Stanford, California 94305 U.S.A.

This paper presents an adjoint method for the optimum shape design of unsteady flows. The goal is to develop a set of discrete unsteady adjoint equations and their corresponding boundary conditions for both the time accurate and non-linear frequency domain methods. First, this paper presents the complete formulation of the time dependent optimal design problem. Second, we present the time accurate and non-linear frequency domain adjoint equations. Third, we present results that demonstrate the application of the theory to a two-dimensional oscillating airfoil. Fourth, we compare the gradients between the two methods.

Introduction

The majority of work in Aerodynamic Shape Optimization (ASO) has been focused on the design of aerospace vehicles which operate in a steady flow environment. Investigators have applied advanced design algorithms, particularly the adjoint method, to numerous structures ranging from the design of two-dimensional airfoils to full aircraft configurations. The redesigned structures exhibit improved performance in the chosen figure of merit including reduced drag, increased range or reduced sonic boom.[9,11,18,20,21] These problems have been tackled using many different numerical schemes on both structured and unstructured grids.[2,6]

There are numerous important engineering applications in which the flow is inherently unsteady but periodic. Helicopter rotors in forward flight, turbomachinery blades and cooling fans operate in unsteady flow and are constantly subjected to unsteady loads. Optimization techniques for unsteady flows are clearly needed to improve their performance, and to alleviate the unsteady effects that contribute to flutter, buffeting, poor gust and acoustic response, and dynamic stall. As yet there have been few efforts in this direction.

One of the major reasons is the demanding computational cost associated with the calculation of unsteady flows. As part of the Accelerated Strategic Computing Initiative (ASCI) project at Stanford, Davis[3] presented estimates for the computational cost of a multistage compressor and turbine calculation based on the parallel execution of 750 processors operating 8 hours a day. He concluded that it would require 1300 days to compute the flow through a 23 blade row compressor. The overwhelming majority of the computational time is spent on time accurately resolving the decay of the initial transients. Although this example is an extreme case, it illustrates the prohibitive cost of many unsteady calculations using time accurate solvers to find a periodic steady state.

Nevertheless, the development of optimum shape design for two-dimensional unsteady flows using the time accurate adjoint based design approach has been pursued by Nadarajah and Jameson.[17,19] They derived and applied the time accurate adjoint equations (both the continuous and discrete) to the redesign of an oscillating airfoil in an inviscid transonic flow. The

*Assistant Professor, Member AIAA
†Post-Doctoral Fellow, Member AIAA
‡Thomas V. Jones Professor of Engineering, Stanford University, AIAA Fellow

redesigned shape achieved a reduction in the time-averaged drag while maintaining the time-averaged lift. The approach utilized a dual time stepping[10] technique that implements a fully implicit second order backward difference formula to discretize the time derivative. Typical runs required 15 periods with 24 discrete time steps per period, and 15 multigrid cycles at each time step. Encouraging results were obtained at a substantial computational expense.

The prohibitive cost of computing three dimensional unsteady flows using the time accurate approach has motivated a new interest in using periodic methods. Linearized frequency domain and deterministic-stress[1] methods are examples of periodic methods. However, these methods generally do not account for strong non-linearities in the system. Pseudo spectral approaches in space and time have been implemented for a multitude of non-linear problems throughout the numerical analysis literature. The Harmonic Balance technique proposed by Hall et. al.[7,8] represents the first pseudo-spectral method in time for the unsteady Euler equations. The Non-Linear Frequency Domain method (NLFD) proposed by McMullen et. al.[14,15] is a similar approach that was later validated for the unsteady Navier-Stokes equations. These approaches are spectral techniques which converge at an exponential rate to the exact solution, even in the presence of aliasing affects.[22] This can be compared to more classical finite difference schemes which contain error proportional to some power of the grid spacing. An analysis presented in McMullen's thesis[16] demonstrates the comparative advantage of spectral techniques for real world applications. Using an unsteady pitching airfoil in a transonic flow, he calculated the error in the magnitude of the fundamental harmonic for the coefficient of lift. The data showed that an NLFD calculation employing one time varying harmonic (which can be represented with three discrete samples) produced an error level equivalent to that of a time accurate calculation using 45 Samples Per Period (SPP). For this case, the NLFD calculation was roughly an order of magnitude more efficient than time accurate codes operating at equivalent error levels.

Recently, there have been two investigations into the modeling of unsteady aerodynamic design sensitivities. Duta et. al.[5] have presented a harmonic adjoint approach for unsteady turbomachinery design. The aim of the work was to reduce blade vibrations due to flow unsteadiness. The research produced adjoint methods that were based on a linearized analysis of periodic unsteady flows. Thomas et. al.[23] presented a viscous discrete adjoint approach for computing unsteady aerodynamic design sensitivities. The adjoint code was generated from the harmonic balance flow solver with the use of an automatic differentiation software compiler.

The motivation of the research in this paper has been fueled both by the success of our current capability for automatic shape optimization for unsteady flows and the future potential of the NLFD method. The general goal of this research is to adapt the NLFD method to the adjoint based design approach. The result of this effort is a NLFD adjoint design code that is fully non-linear and the computational cost of the adjoint module is proportional to the cost of the flow solver. The specific objectives of this work are:

1. Develop the non-linear frequency domain adjoint equations.
2. Validate the time accurate and non-linear frequency domain flow and adjoint solvers.
3. Verify the equivalence of the gradients of the two methods for a time-averaged drag minimization problem.
4. Compare the computational cost of the two approaches.
5. Demonstrate the capability of the design method to achieve significant drag reduction.

Governing Equations

The Euler equations for a rigidly translating control volume Ω, defined by boundary $\partial\Omega$ with an outward facing normal N, can be written in integral form as

$$\frac{d}{dt}\iint_{\Omega} w dx dy + \oint_{\partial\Omega} F_i N_i ds = 0. \qquad (1)$$

The state vector w, and a component of the inviscid flux vector, F_i, can be written as

$$w = \begin{Bmatrix} \rho \\ \rho u_1 \\ \rho u_2 \\ \rho E \end{Bmatrix}, \quad F_i = \begin{Bmatrix} \rho\left(u_i - b_i\right) \\ \rho u_1\left(u_i - b_i\right) + \delta_{1i} p \\ \rho u_2\left(u_i - b_i\right) + \delta_{2i} p \\ \rho E\left(u_i - b_i\right) + p u_i \end{Bmatrix}.$$

In these equations, ρ is the density, x, y are the Cartesian coordinates, u_i, b_i are the Cartesian velocity components of the fluid and boundary respectively, and E is the total energy. The results presented in this paper are based on transonic flow calculations where the ideal gas equation is applicable. Consequently, the pressure, p, can be expressed as

$$p = (\gamma - 1)\,\rho\left\{E - \frac{1}{2}\left(u_i u_i\right)\right\}.$$

Semi-Discrete Form of Governing Equations

The continuous surface integral in equation (1) is represented by a discrete summation of fluxes across a finite number of faces on a control volume.

$$\oint_{\partial\Omega} F_i N_i ds = \sum_{cv} F_i S_i.$$

The approximation of the flux vector, F, that ensures numerical stability is the subject of shock capturing theory. The convective component of the flux is evaluated at the face of the control volume using averages of the flux vector evaluated at the cell centers adjacent to the face. The dissipative component of the flux is a blended mix of first and third order fluxes first introduced by Jameson, Schmidt and Turkel.[12]

$$D_{i+\frac{1}{2},j} = \epsilon^2_{i+\frac{1}{2},j}(w_{i+1,j} - w_{i,j}) - \epsilon^4_{i+\frac{1}{2},j}(w_{i+2,j} - 3w_{i+1,j} + 3w_{i,j} - w_{i-1,j}). \quad (2)$$

The first term in equation (2) is the first order diffusion term, where $\epsilon^2_{i+\frac{1}{2},j}$ is proportional to the normalized second derivative of pressure. This term is dominant in the vicinity of shocks and serves to damp oscillations and overshoots associated with this discontinuity in the solution field. The $\epsilon^4_{i+\frac{1}{2},j}$ coefficient scales the magnitude of the third order dissipative flux. The coefficient is scaled so that it becomes the dominant term away from the shock eliminating the odd-even decoupling associated with central difference schemes. The discrete spatial operator, R, is introduced to include both the convective and dissipative fluxes. The governing equations can be simplified as

$$\frac{d}{dt}\int\int_{\Omega} w dx dy + R = 0. \quad (3)$$

The simulations contained in this research are restricted to rigid mesh translation. Consequently, the volumetric integral can be approximated as the product of the cell volume and the temporal derivative of the solution at the cell center. In semi-discrete form equation (3) can be written as

$$V\frac{\partial w}{\partial t} + R = 0. \quad (4)$$

Formulation of the Time-Dependent Optimal Design Problem

Optimal control of time dependent trajectories is generally complicated by the need to solve the adjoint equation in reverse time from a final boundary condition using data from the trajectory solution, which in turn depends on the control derived from the adjoint solution.

Introduce the cost function

$$I = \int_0^{t_f} \mathcal{L}(w, f)dt + \mathcal{M}(w(t_f)),$$

where the function $\mathcal{L}$ depends on the flow solution w, and the shape function f and the function $\mathcal{M}$ depends on the time dependent flow solution. Assume that the following equation defines the time-dependent flow solution

$$V\frac{\partial w}{\partial t} + R(w, f) = 0,$$

where V is the cell volume and R represents a residue containing the convective and dissipative fluxes. A change in f results in a change

$$\delta I = \int_0^{t_f} \left(\frac{\partial \mathcal{L}^T}{\partial w}\delta w + \frac{\partial \mathcal{L}^T}{\partial f}\delta f\right) dt + \frac{\partial \mathcal{M}^T}{\partial w}\delta w(t_f),$$

in the cost function. The variation in the flow solution is

$$V\frac{\partial}{\partial t}\delta w + \frac{\partial R}{\partial w}\delta w + \frac{\partial R}{\partial f}\delta f = 0.$$

Next, introduce a Lagrange multiplier ψ to the time-dependent flow equation, integrate it over time and subtract it from the variation of the cost function to arrive at the following equation.

$$\begin{aligned}\delta I &= \int_0^{t_f} \left(\frac{\partial \mathcal{L}^T}{\partial w}\delta w + \frac{\partial \mathcal{L}^T}{\partial f}\delta f\right) dt + \frac{\partial \mathcal{M}^T}{\partial w}\delta w(t_f) \\ &- \int_0^{t_f} \psi^T \left(V\frac{\partial}{\partial t}\delta w + \frac{\partial R}{\partial w}\delta w + \frac{\partial R}{\partial f}\delta f\right) dt.\end{aligned}$$

By integrating the term $\int_0^{t_f} \psi^T V\frac{\partial}{\partial t}\delta w dt$ by parts, yields

$$\begin{aligned}\delta I &= \int_0^{t_f} \left(\frac{\partial \mathcal{L}^T}{\partial w} + V\frac{\partial \psi^T}{\partial t} - \psi^T\frac{\partial R}{\partial w}\right)\delta w dt \\ &+ \left(\frac{\partial \mathcal{M}^T}{\partial w} - \psi^T(t_f)\right)\delta w(t_f) \\ &+ \int_0^{t_f} \left(\frac{\partial \mathcal{L}^T}{\partial f} - \psi^T\frac{\partial R}{\partial f}\right)\delta f dt.\end{aligned}$$

Choose ψ to satisfy the adjoint equation

$$V\frac{\partial \psi}{\partial t} = \left(\frac{\partial R}{\partial w}\right)^T \psi - \left(\frac{\partial \mathcal{L}}{\partial w}\right)$$

with the terminal boundary condition

$$\psi(t_f) = \frac{\partial \mathcal{M}}{\partial w}.$$

Then

$$\delta I = \mathcal{G}^T\delta f,$$

where

$$\mathcal{G}^{\mathcal{T}} = \int_0^{t_f} \left(\frac{\partial \mathcal{L}^T}{\partial f} - \psi^T\frac{\partial R}{\partial f}\right) dt.$$

The sensitivity derivatives are determined by the solution of the adjoint equation in reverse time from the terminal boundary condition and the time-dependent solution of the flow equation. These sensitivity derivatives are then used to get a direction of improvement and steps are taken until convergence is achieved.

The computational costs of unsteady optimization problems are directly proportional to the desired number of time steps. The unsteady flow calculation can be obtained either by the use of implicit time-stepping schemes or a NLFD approach.

Development of the Time Accurate Unsteady Discrete Adjoint Equations

This section illustrates application of control theory to unsteady aerodynamic design problems for the case of two-dimensional airfoil design using the compressible Euler equations as the mathematical model.

The unsteady discrete adjoint equation is obtained by applying control theory directly to the set of unsteady discrete field equations. The resulting equation depends on the type of scheme used to solve the flow equations.

A fully-implicit representation of the semi-discrete form of the governing equations (4) can be written as

$$V_{i,j} D_t w_{i,j}^{n+1} + R(w_{i,j}^{n+1}) = 0, \tag{5}$$

where D_t denotes a backward difference approximation to the temporal derivative. A second order expansion of equation (5) will result in the following expression

$$\frac{V_{i,j}}{\Delta t}\left[\frac{3}{2}w_{i,j}^{n+1} - 2w_{i,j}^{n} + \frac{1}{2}w_{i,j}^{n-1}\right] + R(w_{i,j}^{n+1}) = 0. \tag{6}$$

The full unsteady residual, $R^*(w_{i,j})$, represents the summation of both temporal and spatial operators.

$$R^* = \frac{V_{i,j}}{\Delta t}\left[\frac{3}{2}w_{i,j}^{n+1} - 2w_{i,j}^{n} + \frac{1}{2}w_{i,j}^{n-1}\right] + R(w_{i,j}^{n+1}). \tag{7}$$

This paper introduces a pseudo time derivative in conjunction with a multistage explicit Runge-Kutta scheme to minimize the unsteady residual at the completion of each physical time step

$$\frac{\partial w_{i,j}^{n+1}}{\partial \tau} + R_{i,j}^{*^{n+1}} = 0. \tag{8}$$

In addition, established convergence acceleration methods for nonlinear equations, like multigrid and residual averaging, were applied to improve the computational efficiency of the numerical method.

To develop the time accurate discrete adjoint equation, the first step is to take a variation of the modified residual represented in equation (7) with respect to the state vector, w and shape function, f (only terms that are multiplied by δw are shown) to produce

$$\delta R_{i,j}^{*^{n+1}} = \frac{V_{i,j}}{\Delta t}\left[\frac{3}{2}\delta w_{i,j}^{n+1} - 2\delta w_{i,j}^{n} + \frac{1}{2}\delta w_{i,j}^{n-1}\right] + \delta R_{i,j}(w^{n+1}). \tag{9}$$

Multiply the above equation by the transpose of the Lagrange Multiplier and sum over the domain and time to yield

$$\sum_{n=0}^{N}\sum_{\Omega}\psi_{i,j}^{T}\delta R_{i,j}^{*}(w) = \cdots + \psi_{i,j}^{T^{n+1}}\delta R_{i,j}^{*^{n+1}}(w) + \psi_{i,j}^{T^{n+2}}\delta R_{i,j}^{*^{n+2}}(w) + \psi_{i,j}^{T^{n+3}}\delta R_{i,j}^{*^{n+3}}(w) + \cdots,$$

where $N = \frac{t_f}{\Delta t}$ and t_f is the final or total time. Substitute equation (9) into the $(n+1)$, $(n+2)$, and $(n+3)$ terms of the modified residual in the above equation to yield

$$\begin{aligned}
&\sum_{n=0}^{N}\sum_{\Omega}\psi_{i,j}^{T}\delta R_{i,j}^{*}(w) = \cdots \\
&+\psi_{i,j}^{T^{n+1}}\frac{V_{i,j}}{\Delta t}\left[\frac{3}{2}\delta w_{i,j}^{n+1} - 2\delta w_{i,j}^{n}(w) + \frac{1}{2}\delta w_{i,j}^{n-1}\right] \\
&\quad +\psi_{i,j}^{T^{n+1}}\delta R_{i,j}^{n+1} \\
&+\psi_{i,j}^{T^{n+2}}\frac{V_{i,j}}{\Delta t}\left[\frac{3}{2}\delta w_{i,j}^{n+2} - 2\delta w_{i,j}^{n+1}(w) + \frac{1}{2}\delta w_{i,j}^{n}\right] \\
&\quad +\psi_{i,j}^{T^{n+2}}\delta R_{i,j}^{n+2} \\
&+\psi_{i,j}^{T^{n+3}}\frac{V_{i,j}}{\Delta t}\left[\frac{3}{2}\delta w_{i,j}^{n+3} - 2\delta w_{i,j}^{n+2}(w) + \frac{1}{2}\delta w_{i,j}^{n+1}\right] \\
&\quad +\psi_{i,j}^{T^{n+3}}\delta R_{i,j}^{n+3} + \cdots.
\end{aligned}$$

Keeping only the $\delta w_{i,j}^{n+1}$ terms, rearrange the terms in the equation to produce the time accurate discrete adjoint equation

$$\begin{aligned}
&\sum_{n=0}^{N}\sum_{\Omega}\psi_{i,j}^{T}\delta R_{i,j}^{*}(w) = \cdots \\
&+\left[\frac{3}{2\Delta t}\psi_{i,j}^{T^{n+1}} - \frac{2}{\Delta t}\psi_{i,j}^{T^{n+2}} + \frac{1}{2\Delta t}\psi_{i,j}^{T^{n+3}}\right] V_{i,j}\delta w_{i,j}^{n+1} \\
&\quad +\psi_{i,j}^{T^{n+1}}\delta R_{i,j}^{n+1} + \cdots.
\end{aligned} \tag{10}$$

Next we introduce the discrete cost function for the drag minimization problem as

$$\begin{aligned}
I_c &= \frac{1}{t_f}\sum_{n=0}^{N} C_d\,\Delta t \\
&= \frac{\eta}{t_f}\sum_{n=0}^{N}\sum_{i=LTE}^{UTE} p_{i,W}\left(\frac{\Delta y_i}{\Delta s_i}\cos\alpha - \frac{\Delta x_i}{\Delta s_i}\sin\alpha\right)\Delta s_i \Delta t,
\end{aligned}$$

where $\eta = \frac{1}{\frac{1}{2}\gamma P_\infty M_\infty^2 \bar{c}}$, LTE is the lower trailing edge, UTE is the upper trailing edge, Δs_i is the surface cell arc length, and $\Delta p_{i,W}$ is the wall pressure. In this research the wall pressure is defined as such

$$p_{i,W} = \frac{1}{2}\left(p_{i,2} + p_{i,1}\right) - p_\infty,$$

where $p_{i,2}$ is the value of the pressure in the cell above the wall and $p_{i,1}$ is the value of the pressure in the cell

below the wall. A variation in the cost function will result in a variation, Δp, in the pressure and variations, Δy and Δx, in the geometry. The variation of the cost function for drag minimization can be written as

$$\begin{aligned}\delta I_c &= \frac{\eta}{t_f}\sum_{n=0}^{N}\left[\sum_{i=LTE}^{UTE}\frac{1}{2}\left(\frac{\Delta y_i}{\Delta s_i}\cos\alpha-\frac{\Delta x_i}{\Delta s_i}\sin\alpha\right)\bullet\right.\\ &\qquad \frac{\partial p}{\partial w}\left(\delta w_{i,2}+\delta w_{i,1}\right)\Delta s_i\\ &\quad +\sum_{i=LTE}^{UTE}\left(\frac{1}{2}\left(p_{i,2}+p_{i,1}\right)-p_\infty\right)\bullet\\ &\qquad \left.[\cos\alpha\,\delta\left(\Delta y_i\right)-\sin\alpha\,\delta\left(\Delta x_i\right)]\right]\Delta t. \quad (11)\end{aligned}$$

The time dependent discrete Euler equations can now be introduced into δI as a constraint to produce

$$\delta I=\delta I_c-\sum_{n=0}^{N}\sum_{\Omega}\psi_{i,j}^{T}\delta R_{i,j}^{*}(w).$$

Substitute equation (10) and (11) into the above expression to yield

$$\begin{aligned}\delta I &= \frac{\eta}{t_f}\sum_{n=0}^{N}\left[\sum_{i=LTE}^{UTE}\frac{1}{2}\left(\frac{\Delta y_i}{\Delta s_i}\cos\alpha-\frac{\Delta x_i}{\Delta s_i}\sin\alpha\right)\bullet\right.\\ &\qquad \frac{\partial p}{\partial w}\left(\delta w_{i,2}+\delta w_{i,1}\right)\Delta s_i\\ &\quad +\sum_{i=LTE}^{UTE}\left(\frac{1}{2}\left(p_{i,2}+p_{i,1}\right)-p_\infty\right)\bullet\\ &\qquad \left.[\cos\alpha\,\delta\left(\Delta y_i\right)-\sin\alpha\,\delta\left(\Delta x_i\right)]\right]\Delta t\\ &\quad -\frac{1}{\Delta t}\left[\frac{3}{2}\psi_{i,j}^{T^{n+1}}-2\psi_{i,j}^{T^{n+2}}+\frac{1}{2}\psi_{i,j}^{T^{n+3}}\right]V_{i,j}\delta w_{i,j}^{n+1}\\ &\quad +\psi_{i,j}^{T^{n+1}}\delta R_{i,j}^{n+1}\end{aligned}$$

The above expression can be rearranged into two main categories: first, terms that are multiplied by the variation of the state vector, δw; and second, terms that are multiplied by the variation of the shape function, δf. The rearranged equation can be expressed as

$$\begin{aligned}\delta I=\cdots &+ \frac{1}{2}\left(\frac{\Delta y_i}{\Delta s_i}\omega\cos\alpha-\frac{\Delta x_i}{\Delta s_i}\omega\sin\alpha\right)\bullet\\ &\qquad \frac{\partial p}{\partial w}\left(\delta w_{i,2}^{n+1}+\delta w_{i,1}^{n+1}\right)\Delta s_i\Delta t\\ &- \frac{1}{\Delta t}\left[\frac{3}{2}\psi_{i,j}^{T^{n+1}}-2\psi_{i,j}^{T^{n+2}}+\frac{1}{2}\psi_{i,j}^{T^{n+3}}\right]V_{i,j}\delta w_{i,j}^{n+1}\\ &\qquad -\psi_{i,j}^{T^{n+1}}\delta_w R_{i,j}^{n+1}\\ &- \psi_{i,j}^{T^{n+1}}\delta_f R_{i,j}^{n+1}+\left(\frac{1}{2}\left(p_{i,2}+p_{i,1}\right)-p_\infty\right)\bullet\\ &\qquad [\delta\left(\Delta y_i\right)\eta\cos\alpha-\delta\left(\Delta x_i\right)\eta\sin\alpha]\,\Delta t+\cdots, \quad (12)\end{aligned}$$

where $\delta_w R_{i,j}^{n+1}$ are terms that are a result of taking a variation of the residual with respect to the state vector, w, and $\delta_f R_{i,j}^{n+1}$ are terms that are a result of taking a variation of the residual with respect to the shape function, f. Equation (12) can be further expanded to isolate the $\delta w_{i,2}^{n+1}$ terms. This step is needed to produce the boundary condition source term for the time accurate discrete adjoint equation. The extraction of the $\delta w_{i,2}^{n+1}$ term results in the following split in the equation

$$\begin{aligned}\delta I &= \cdots\\ &\quad +\frac{1}{2}\left(\frac{\Delta y_i}{\Delta s_i}\eta\cos\alpha-\frac{\Delta x_i}{\Delta s_i}\eta\sin\alpha\right)\frac{\partial p}{\partial w}\delta w_{i,1}^{n+1}\Delta s_i\Delta t\\ &\quad +\frac{1}{2}\left(\frac{\Delta y_i}{\Delta s_i}\eta\cos\alpha-\frac{\Delta x_i}{\Delta s_i}\eta\sin\alpha\right)\frac{\partial p}{\partial w}\delta w_{i,2}^{n+1}\Delta s_i\Delta t\\ &\quad -\frac{1}{\Delta t}\left[\frac{3}{2}\psi_{i,2}^{T^{n+1}}-2\psi_{i,2}^{T^{n+2}}+\frac{1}{2}\psi_{i,2}^{T^{n+3}}\right]V_{i,j}\delta w_{i,2}^{n+1}\\ &\qquad -\psi_{i,2}^{T^{n+1}}\delta_w R_{i,2}^{n+1}\\ &\quad -\frac{1}{\Delta t}\left[\frac{3}{2}\psi_{i,j}^{T^{n+1}}-2\psi_{i,j}^{T^{n+2}}+\frac{1}{2}\psi_{i,j}^{T^{n+3}}\right]V_{i,j}\delta w_{i,j}^{n+1}\\ &\qquad -\psi_{i,j}^{T^{n+1}}\delta_w R_{i,j}^{n+1}\\ &\quad -\psi_{i,j}^{T^{n+1}}\delta_f R_{i,j}^{n+1}+\left(\frac{1}{2}\left(p_{i,2}+p_{i,1}\right)-p_\infty\right)\bullet\\ &\qquad [\delta\left(\Delta y_i\right)\eta\cos\alpha-\delta\left(\Delta x_i\right)\eta\sin\alpha]\,\Delta t+\cdots \quad (13)\end{aligned}$$

A brief explanation of the steps taken in the above equation is needed here. First, the first line in equation (12) is split into $\delta w_{i,1}^{n+1}$ and $\delta w_{i,2}^{n+1}$ resulting in the first and second line in the above equation. Second, $\delta w_{i,2}^{n+1}$ is extracted from the second lines in equation (12) to produce the third and fourth lines in the above equation. The last line in the above equation remains as is. To establish the drag minimization boundary condition source term for the time accurate discrete adjoint equation, we first need to expand the $\delta_w R_{i,2}^{n+1}$ term. From equation (13), the $\delta_w R_{i,2}^{n+1}$ term can be written as follows

$$\begin{aligned}\psi_{i,2}^{T^{n+1}}\delta_w R_{i,2}^{n+1} = &- \frac{1}{2}\left[A_{i-\frac{1}{2},2}^{T^{n+1}}\left(\psi_{i,2}^{n+1}-\psi_{i-1,2}^{n+1}\right)\right.\\ &\quad +A_{i+\frac{1}{2},2}^{T^{n+1}}\left(\psi_{i+1,2}^{n+1}-\psi_{i,2}^{n+1}\right)\\ &\quad +B_{i,\frac{5}{2}}^{T^{n+1}}\left(\psi_{i,3}^{n+1}-\psi_{i,2}^{n+1}\right)\\ &\quad \left.-\Delta y_\xi\psi_{2_{i,2}}^{n+1}+\Delta x_\xi\psi_{3_{i,2}}^{n+1}\right]\delta w_{i,2}^{n+1}.\end{aligned}$$

The time accurate discrete adjoint equation can now be defined as

$$\begin{aligned}&\frac{\partial\psi_{i,j}^{n+1}}{\partial\tau}-\frac{1}{\Delta t}\left[\frac{3}{2}\psi_{i,j}^{T^{n+1}}-2\psi_{i,j}^{T^{n+2}}+\frac{1}{2}\psi_{i,j}^{T^{n+3}}\right]V_{i,j}\\ &\qquad -\psi_{i,j}^{T^{n+1}}\delta_w R_{i,j}^{n+1}=0.\end{aligned}$$

At cell $(i,2)$ the time accurate discrete adjoint equation is as follows,

$$\begin{aligned}&\frac{\partial\psi_{i,2}^{n+1}}{\partial\tau}-\frac{1}{\Delta t}\left[\frac{3}{2}\psi_{i,2}^{T^{n+1}}-2\psi_{i,2}^{T^{n+2}}+\frac{1}{2}\psi_{i,2}^{T^{n+3}}\right]V_{i,j}\\ &-\frac{1}{2}\left[A_{i-\frac{1}{2},2}^{T^{n+1}}\left(\psi_{i,2}^{n+1}-\psi_{i-1,2}^{n+1}\right)+A_{i+\frac{1}{2},2}^{T^{n+1}}\left(\psi_{i+1,2}^{n+1}-\psi_{i,2}^{n+1}\right)\right.\\ &\left.+B_{i,\frac{5}{2}}^{T^{n+1}}\left(\psi_{i,3}^{n+1}-\psi_{i,2}^{n+1}\right)-\Phi\right]=0, \quad (14)\end{aligned}$$

where Φ is the source term for drag minimization,

$$\Phi = \Delta y_\xi \psi_{2_{i,2}}^{n+1} - \Delta x_\xi \psi_{3_{i,2}}^{n+1} + \left(\frac{\Delta y_i}{\Delta s_i} \eta \cos\alpha - \frac{\Delta x_i}{\Delta s_i} \eta \sin\alpha \right) \frac{\partial p}{\partial w} \Delta s_i \Delta t.$$

All the terms in equation (14) except for the source term scale as the square of Δx. Therefore, as the mesh width is reduced, the terms in the source term if divided by Δs_i must approach zero as the solution reaches a steady-state. One then recovers the continuous adjoint boundary condition (Refer to Nadarajah and Jameson[17] for derivation of the time accurate continuous adjoint equation and boundary conditions). Thus equation (13) simplifies to the following equation,

$$\delta I = \cdots - \psi_{i,j}^{T^{n+1}} \delta_f R_{i,j}^{n+1} + \left(\frac{1}{2} \left(p_{i,2} + p_{i,1} \right) - p_\infty \right) \bullet \left[\delta \left(\Delta y_i \right) \eta \cos\alpha - \delta \left(\Delta x_i \right) \eta \sin\alpha \right] \Delta t + \cdots \quad (15)$$

The above equation represents the total gradient obtained using the time accurate discrete adjoint approach to reduce the total drag of a pitching airfoil.

Development of the Non-Linear Frequency Domain Adjoint Equations

The derivation of the NLFD method starts with the semi-discrete form of the governing equations, and assumes that the solution w and spatial operator R can be represented by separate Fourier series:

$$w = \sum_{k=-\frac{N}{2}}^{\frac{N}{2}-1} \hat{w}_k e^{ikt}$$

$$R = \sum_{k=-\frac{N}{2}}^{\frac{N}{2}-1} \hat{R}_k e^{ikt} \quad (16)$$

where,

$$i = \sqrt{-1}. \quad (17)$$

Here, however each coefficient $\hat{R}_k$ of the transform of the residual depends on all the coefficients $\hat{w}_k$, because $R(w(t))$ is a non-linear function of $w(t)$. Thus equation (18) represents a non-linear set of equations which must be iteratively solved. The solver attempts to find a solution, w, that drives this system of equations to zero for all wavenumbers, but at any iteration in the solution process the unsteady residual, R^*, will be finite:

$$\hat{R^*}_k = ikV\hat{w}_k + \hat{R}_k. \quad (18)$$

The nonlinearity of the unsteady residual stems from the spatial operator. There are two approaches to calculating the spatial operator expressed in the frequency domain. The first uses a complex series of convolution sums to calculate $\hat{R}_k$ directly from $\hat{w}_k$. This approach is discarded due to its massive complexity (considering artificial dissipation schemes and turbulence modeling) and cost that scales quadratically with the number of modes N. Instead, we implement a pseudo-spectral approach in time. This approach requires several transformations between the physical and frequency domains which are performed by a Fast Fourier Transform (FFT). The computational cost of this transform scales like $N\log(N)$, where N is a large number. A diagram detailing the transformations used by the pseudo spectral approach is provided in figure (1).

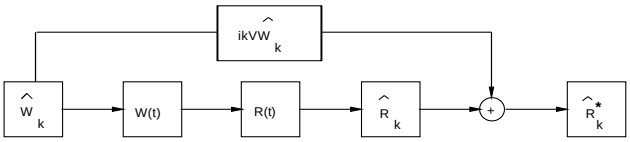

Fig. 1 Simplified dataflow diagram of the time advancement scheme illustrating the pseudo spectral approach used in calculating the non-linear spatial operator R.

The pseudo-spectral approach begins by assuming that $\hat{w}_k$ is known for all wavenumbers. Using an inverse FFT, $\hat{w}_k$ can be transformed back to the physical space resulting in a state vector $w(t)$ sampled at evenly distributed intervals over the time period. At each of these time instances the steady-state operator $R(w(t))$ can be computed. A FFT is then used to transform the spatial operator to the frequency domain where $\hat{R}_k$ is known for all wavenumbers. The unsteady residual $\hat{R^*}_k$ can then be calculated by adding $\hat{R}_k$ to the spectral representation of the temporal derivative $ikV\hat{w}_k$.

Consistent with the time accurate approach, a pseudo-time derivative can be added, and a time-stepping scheme can be employed to numerically integrate the resulting equations.

$$V\frac{\partial \hat{w}_k}{\partial \tau} + \hat{R^*}_k = 0. \quad (19)$$

In the NLFD case, an unsteady residual exists for each wavenumber used in the solution and the pseudo-time derivative acts as a gradient to drive the absolute value of all of these components to zero simultaneously.

The NLFD discrete adjoint equation can be developed using two separate approaches. In the first approach, we first take a variation of the unsteady residual $\hat{R^*}_k$ represented in equation (18) with respect to the state vector $\hat{w}_k$ and shape function f, to produce

$$\delta\hat{R^*}_k = ikV\delta\hat{w}_k + \delta\hat{R}_k.$$

The next step, would be to expand $\delta\hat{R}_k$ as a function of $\hat{w}_k$. As mentioned earlier, this approach would require a series of convolution sums to express $\delta\hat{R}_k$ as a

function of $\delta\hat{w}_k$. This method was not implemented due to its computational cost and added complexity. Instead, the adjoint equations were solved using a pseudo-spectral approach similar to the one applied to the flow equations.

In the latter approach, the NLFD adjoint equations are developed from the semi-discrete from of the adjoint equation, which can be as expressed as

$$V\frac{\partial\psi}{\partial t} + R(\psi) = 0,$$

where $R(\psi)$ is the sum of all the spatial operators, both convective and dissipative, used in the discretized adjoint equations. Refer to Nadarajah[19] for a detailed derivation of these spatial operators and boundary conditions. Next, we assume that the adjoint variable and spatial operator can be expressed as a Fourier series:

$$\begin{aligned} \psi &= \sum_{k=-\frac{N}{2}}^{\frac{N}{2}-1} \hat{\psi}_k e^{ikt}, \\ R(\psi) &= \sum_{k=-\frac{N}{2}}^{\frac{N}{2}-1} \widehat{R(\psi)}_k e^{ikt}. \end{aligned} \tag{20}$$

The derivation of the NLFD adjoint then follows that of the NLFD flow equations. The NLFD adjoint equations are expressed as

$$V\frac{\partial\hat{\psi}_k}{\partial\tau} + \widehat{R(\psi)}_k^* = 0.$$

where $\widehat{R(\psi)}_k^* = ikV\hat{\psi}_k + \widehat{R(\psi)}_k$. The pseudo-spectral approach illustrated in figure (1) is employed in the NLFD adjoint code to form the unsteady residual. This term in conjunction with a pseudo time derivative provides an iterative solution process consistent with that documented for the flow equations.

Design Process

The design process used by this paper will change the shape of the airfoil in order to minimize its time averaged coefficient of drag. Given the derivation provided in previous sections the adjoint boundary condition can easily be modified to admit other figures of merit. The shape of the airfoil is constrained such that the maximum thickness to chord ratio remains constant between the initial and final designs. In addition, the mean angle of attack is allowed to vary to ensure the time averaged coefficient of lift remains constant between designs.

The results section of this paper will compare the results of two separate codes implementing this design process. The first code, UTSYN103 developed by Nadarajah and Jameson,[17,19] employs a time accurate method in the solution of the unsteady Euler equations. The second code, UFSYN103, simply modifies the representation of the temporal derivative in UTSYN103 with the NLFD methods of McMullen et. al.[14–16] For each code, the individual steps within each iteration of the design process are outlined below.

Time Accurate (UTSYN103)

The time accurate adjoint based design procedure requires the following steps:

1. **Time Accurate Flow Calculation at Constant Time Averaged Lift Coefficient**. A multigrid scheme is used to drive the unsteady residual for each time step to a negligible value. The duration of the physical time history (typically quantified in the number of oscillatory periods) depends on the physics of the flow field and the accuracy requirements of the calculation. In the case of a design process where time averaged lift is held constant, the mean angle of attack is then perturbed to ensure consistency in the mean coefficient of lift between designs. For this case, the above process is repeated until the solution at a constant mean angle of attack has converged.

2. **Time Accurate Adjoint Calculation**. The unsteady discrete adjoint equations are solved in reverse time. With minor modifications, the numerical scheme employed to solve the unsteady flow equations is used to solve the adjoint system in reverse time.

3. **Gradient Evaluation**. An integral over the last period of the adjoint solution is used to form the gradient. This gradient is then smoothed using an implicit smoothing technique. This ensures that each new shape in the optimization sequence remains smooth and acts as a preconditioner which allows the use of much larger steps. The smoothing leads to a large reduction in the number of design iterations needed for convergence. Refer to Nadarajah et. al.[17] for a more comprehensive overview of the gradient smoothing technique. An assessment of alternative search methods for a model problem is given by Jameson and Vassberg.[13]

4. **Airfoil Shape Modification**. The airfoil shape is then modified in the direction of improvement using a steepest descent method.

   Let $\mathcal{F}$ represent the design variable, and $\mathcal{G}$ the gradient. An improvement can then be made with a shape change

   $$\delta\mathcal{F} = -\lambda\mathcal{G},$$

5. **Grid Modification**. The internal grid is modified based on perturbations on the surface of the airfoil. The method modifies, the grid points along each grid index line projecting from the surface. The arc length between the surface point and the far-field point along the grid line is first computed, then the grid point at each location along the grid line is attenuated proportional to the ratio of its arc length distance from the surface point and the total arc length between the surface and the far-field.

6. **Repeat the Design Process**. The entire design process is repeated until the objective function converges. The problems in this work typically required between nine to twenty five design cycles to reach the optimum.

Non-Linear Frequency Domain (UFSYN103)

The NLFD adjoint based design procedures require the following steps:

1. **Periodic Flow Calculation at Constant Time Averaged Lift**. A set of multigrid cycles is used to drive the unsteady residual to a negligible value for all the modes used in the representation of the solution. In the case of a design process that constrains the time averaged lift, the mean angle of attack is perturbed every 10 multigrid cycles to maintain a constant time averaged coefficient of lift. This allows the unsteady residual to reduce by an order to two in magnitude before the angle is modified again.

2. **Adjoint Calculation**. The adjoint equation is solved by integrating in reverse time. With minor modifications, the NLFD numerical scheme employed to solve the flow equations is used to solve the adjoint equations in reverse time.

3-6. These steps are identical to the steps enumerated for the time accurate version of the code.

Results

The following sections present results from simulations of a two-dimensional airfoil undergoing a change in angle of attack as a function of time.

$$\alpha(t) = \alpha_o + \alpha_m \sin(\omega t),$$

For all the cases presented in this section, the mean angle of attack, α_o is 0 degrees and the maximum dynamic angle of attack, α_m, is 1.01 degrees. The reduced frequency, $\frac{\omega c}{2V_\infty}$, for these simulations was 0.202, with a far-field Mach number, M_∞, of 0.78. These boundary conditions match the conditions used by Davis[4] in case CT6 of his experimental survey.

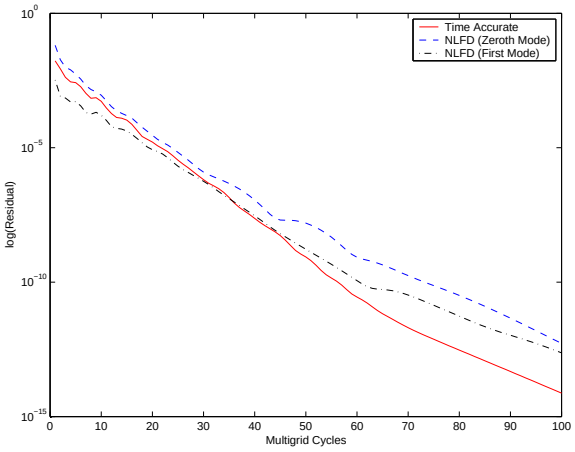

Fig. 2 Convergence History of the Time Accurate and NLFD Adjoint Solvers for the RAE 2822 Airfoil.

The first part of the results section contains a code validation study. This study compares the adjoint solutions from both the time accurate and NLFD codes. The second section is dedicated to a gradient accuracy study for the two approaches. The third section contains results of the redesign of the RAE 2822 airfoil to reduce the time-averaged drag coefficient without a constraint on the time averaged coefficient of lift. The final section produces a similar case study with the lift constrained.

Validation

This section compares the adjoint solutions from the time accurate and NLFD codes. These solutions are based on a 193x33 mesh of a RAE 2822 airfoil. The time accurate code used a temporal resolution of 23 Samples Per Period (SPP) while the NLFD code used only one time varying harmonic (corresponding to three SPP). The temporal resolutions for both codes were selected using the gradient surveys presented in the following section.

Figure (2) shows convergence of the adjoint unsteady residual as a function of the multigrid cycle for each code. The time accurate results show the residual decay for only one step in the dual time stepping process. The decay rates of the residual for other steps throughout the time history of the calculation are similar. Both the NLFD and time accurate methods produce similar decay rates of the residual per multigrid cycle. Both residual modes within the NLFD calculation converge at similar rates. For most cases, the initial residual of the time accurate solver is one or two orders of magnitude less than the initial residual for the NLFD solver.

Comparisons of the adjoint solutions, using the same temporal resolutions referenced above, are provided in figures (3-6). The figures compare the time average of the adjoint variable at the surface of the airfoil for both codes. All four figures show excellent agreement

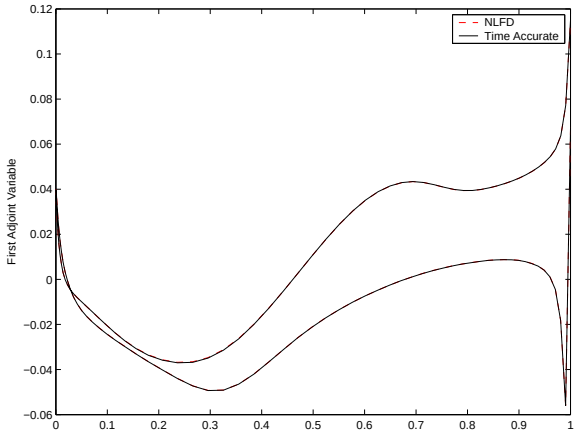

Fig. 3 Time average of the first adjoint variable at the wall of the airfoil produced by the NLFD (3 SPP) and time accurate (23 SPP) codes.

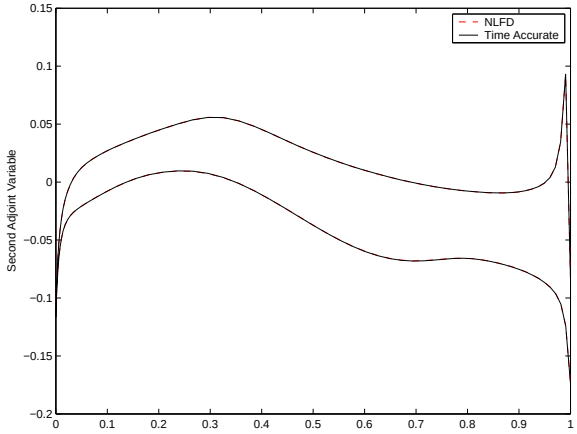

Fig. 4 Time average of the second adjoint variable at the wall of the airfoil produced by the NLFD (3 SPP) and time accurate (23 SPP) codes.

with no visual difference between the two methods for each adjoint variable.

Gradient Study

This section compares the gradients produced by the NLFD and time accurate methods. The gradients are computed at the end of a single design cycle that starts with an RAE 2822 airfoil. The spatial resolution remains fixed with identical 193x33 grids being employed for all calculations. However, the number of samples per temporal period will vary to show the accuracy of the gradient

In figure (7), we compare the gradients produced by the NLFD method using a varying number of temporal modes (includes 1, 2, 4 and 11 modes cases). At each design cycle, 100 multigrid cycles are employed to solve the unsteady flow and adjoint residuals. For the NLFD flow solver, a seven order of magnitude reduction in the unsteady residual is attained and a 14 order magnitude reduction for the adjoint solver. The rapid convergence of gradient is demonstrated by the close agreement of the results over the range in temporal resolutions.

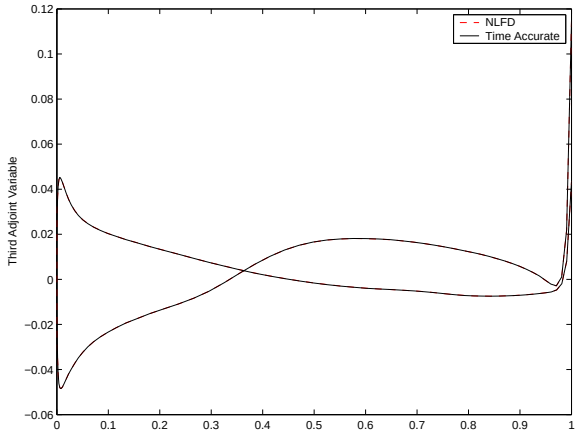

Fig. 5 Time average of the third adjoint variable at the wall of the airfoil produced by the NLFD (3 SPP) and time accurate (23 SPP) codes.

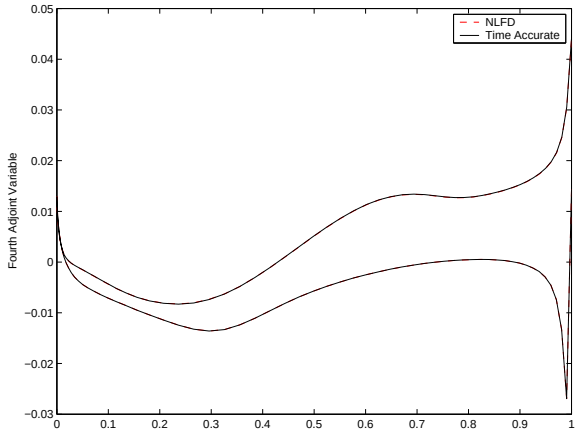

Fig. 6 Time average of the fourth adjoint variable at the wall of the airfoil produced by the NLFD (3 SPP) and time accurate (23 SPP) codes.

A more quantitative comparison of the temporal accuracy of the gradient begins with the selection of a control solution using the highest temporal resolution. This study uses the gradients produced from the 11 mode NLFD calculation as the control. Gradients from all other calculations, both NLFD and time accurate, will be subtracted from this control to quantify error.

In table (1), we show the norm of the difference between the control and gradients computed using various temporal resolutions of the NLFD method. The one mode case produces a highly accurate gradient that is within $2.5e-4$ of the control solution. The numbers justify the assertion that temporal convergence is achieved using just one time varying mode.

Figure (8) shows the gradients produced by a time accurate method over a variety of temporal resolutions. These cases included using 3, 5, 9, 23, and 36 SPP for both the flow and adjoint solutions. All the cases, calculate 25 periods for both of these solutions. This ensured that a periodic steady state solution was

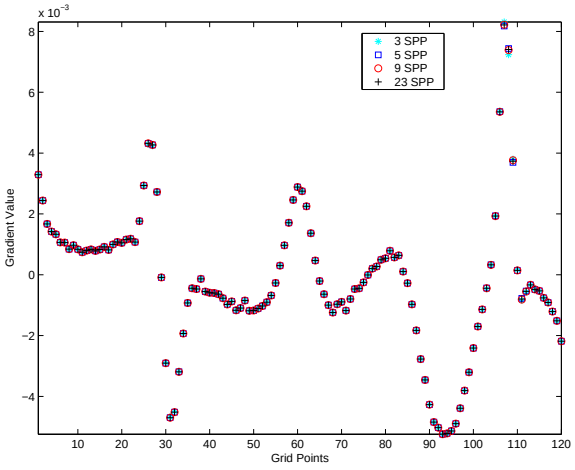

Fig. 7 Comparison of Gradient for Various Numbers of Time Samples per Period for the RAE 2822 Airfoil Mesh using the NLFD method.

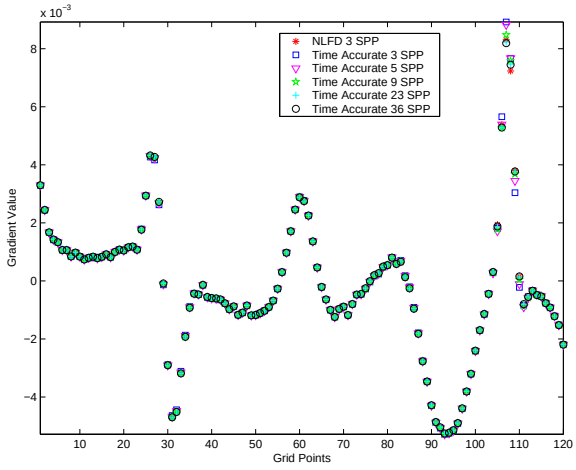

Fig. 8 Comparison of Gradient for Various Number of Time Samples per Period for the RAE 2822 Airfoil Mesh using the Time Accurate method.

SPP	Time Varying Modes	Norm of the Difference
3	(1)	$2.4877e-04$
5	(2)	$6.9388e-05$
9	(4)	$4.4930e-05$

Table 1 Gradient Convergence for Various Temporal Resolutions Used by the NLFD approach

SPP	Norm of the Difference
3	$1.1900e-03$
5	$8.8763e-04$
9	$5.4650e-04$
23	$3.7743e-04$
36	$3.7040e-04$

Table 2 Gradient Convergence for Various SPP for the Time Accurate approach

obtained, eliminating any error associated with initial transients. For each of these cases, the change in the time-averaged lift coefficient from one period to the next was within $1.E-6$. At each time step, 100 multigrid cycles are employed to solve the unsteady flow and adjoint residuals. This corresponds to a reduction in the unsteady residual by seven orders of magnitude for the flow and 14 orders of magnitude for the adjoint.

The time accurate gradients show excellent agreement for all grid points except between the 105th and 110th points. These points lie in the region of the shock wave and produce the largest gradient values. A closer inspection of the data, reveals that these points converge as the temporal resolution is increased.

In figure (8), we compare the gradient computed from the lowest resolution NLFD solution against all of the time accurate gradients. Away from the shock the different codes provide results that match to plotting accuracy. At the shock, the low resolution NLFD results are in close agreement with the highest resolution of time accurate results.

In table (2), we provide the norm of the difference between the gradient obtained from the different temporal resolutions of time accurate calculations and the control solution. As the temporal resolution of the time accurate approach is increased, the norm of the difference between the two gradients decreases as expected.

A comparison of tables (1) and (2) show that the gradient produced from a single mode NLFD case is roughly as accurate as the gradient produced from a 23 SPP time accurate calculation. These temporal resolutions were chosen as the standard for the other surveys documented by this paper. This ensures that other comparisons will use gradient accuracy levels that are roughly equivalent between the two methods.

RAE 2822: Time-Averaged Drag Minimization without Fixed Lift Constraint

This section documents the results of the redesign of the RAE 2822 airfoil without imposing any constraints on the time average lift. The time accurate approach used 50 design cycles in each of which the flow and adjoint solutions were calculated over 20 physical time periods. The temporal resolution was 23 SPP. 50 multigrid cycles were used for each time instance to ensure full convergence of the unsteady residual. The NLFD computation also used 50 design cycles. However, the adjoint and flow solutions were resolved with only 3 SPP. 100 multigrid cycles were used to drive all modes of the unsteady residual to a negligible value.

Figure 9 compares the final airfoil geometries for the two approaches. The location of the final optimized surfaces agrees to plotting accuracy. The norm of the difference between the two final airfoils is $2.2288e-04$. In figure (10) the initial and final airfoil geometries obtained with the NLFD method are compared. A distinctive feature of the new airfoil is the drastic

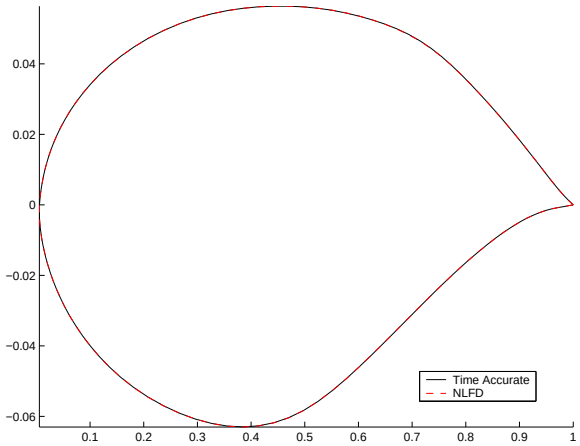

Fig. 9 Comparison Between the Final Geometries Produced by the Time Accurate and NLFD Methods.

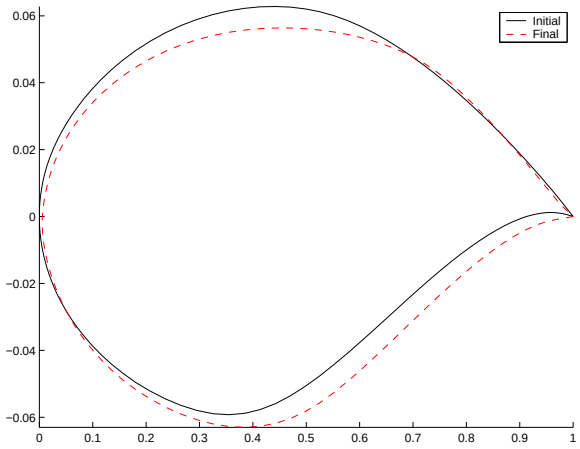

Fig. 10 Comparison Between the Initial and Final Geometries Produced by the NLFD Method.

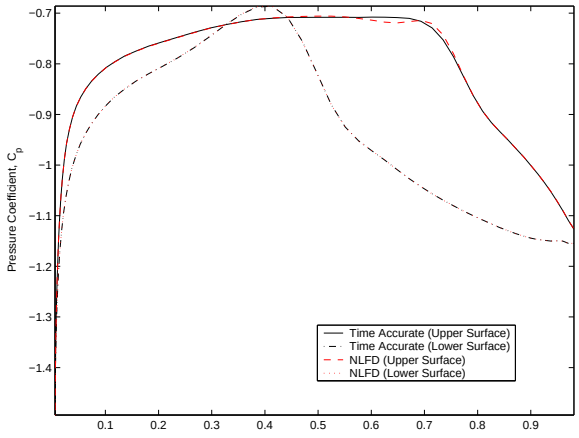

Fig. 11 Comparison of the Final Pressure Distribution Between the Time Accurate and NLFD Method without Lift Constraints.

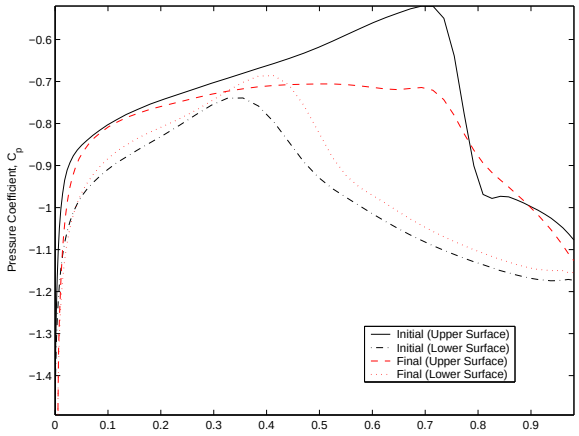

Fig. 12 Comparison of the Initial and Final Pressure Distribution using the NLFD method without Lift Constraints.

reduction of the upper surface curvature. Pressure distributions shown later in this section will show this reduced curvature leads to a weaker shock and lower wave drag. However, the unconstrained design process decambers the airfoil, which results in a loss of lift.

Figure (11) shows a comparison of the surface pressure distribution for the redesigned airfoil based on the time-averaged solutions from the two approaches. The pressure distributions show excellent agreement between the two methods. Only a slight difference is noticed at the location of the shock on the upper surface.

Figure (12) shows a comparison of the initial and final surface pressure distributions based on the time-averaged solution obtained from the NLFD approach. The plot illustrates the severe weakening of the upper shock, which results in a drastic reduction in the drag coefficient.

Finally, we compare the convergence of the cost function for the two methods in figure (13). The temporal resolutions of each solver were chosen to ensure gradients of equivalent accuracy. Given similar gradients, it is not surprising that the cost functions converge at almost identical rates. Both the NLFD and time accurate approaches converge to the final time-averaged drag coefficient in 35 design cycles.

RAE 2822: Time-Averaged Drag Minimization with Fixed Time-Averaged Lift Coefficient

In this section, we repeat the optimization of the RAE 2822 airfoil from the previous section but impose a constraint on the time-averaged lift coefficient. This coefficient is held constant by modifying the mean angle of attack. For the time accurate case, changing the angle of attack requires additional periods to eliminate the initial transients introduced by this change. For this case the mean angle of attack was perturbed every six periods. Consequently the constrained design process required a total of 42 periods in comparison with 20 used for the unconstrained case presented in the previous section. These time accurate calculations used 23 SPP, and 50 multigrid cycles per discrete time step. The magnitude of the unsteady residual decreased by seven orders of magnitude for the flow solver and 14 for the adjoint.

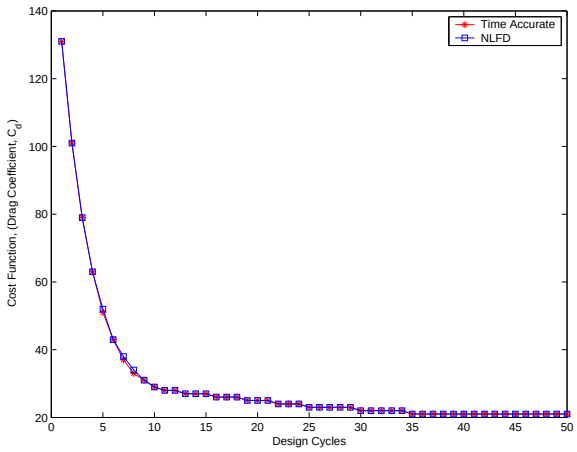

Fig. 13 Comparison of the Convergence of the Cost Function for the Time Accurate and NLFD methods without Lift Constraints.

For the NLFD case, the mean angle of attack was modified every 10 multigrid cycles. One hundred multigrid cycles were used for the flow and adjoint solvers achieving similar reductions in the residuals as is in the time accurate case.

Figure (14) shows a comparison of the final airfoil geometry between the time accurate and NLFD methods. Both approaches produce nearly identical geometries. The norm of the difference between the two final airfoils is $1.1928e-04$. In figure (15), we show the initial and final airfoil geometries produced by the NLFD approach. The reduction of the upper surface curvature as seen in the previous case is evident here as well.

Figure (16) shows a comparison between the surface pressure distributions based on the time-averaged flow solution. Both approaches produce almost identical pressure distributions with minor differences in the area of the shock wave. Figure (17) shows the difference between the initial and final pressure distributions computed by the NLFD technique. The large reduction in the strength of the upper shock is illustrated by the reduction in the surface pressure gradient in this area.

Figure (18), shows the convergence of the cost function, the time-averaged drag coefficient, as a function of the design cycle. The final design is obtained within 18 design cycles and achieves a 57 percent reduction in the time-averaged drag coefficient. As with the unconstrained case, both techniques produce almost identical convergence histories.

Conclusion

Our main conclusion is that the NLFD and time accurate methods produce essentially identical results, but the NLFD method has a much lower computational cost for periodic unsteady problems of this nature. This can be attributed to the convergence rate of the multigrid scheme used to solve the NLFD equations which is essentially the same as the convergence rate for the solution of the backward difference formula in the time accurate method. Both methods achieved a 57 percent reduction in the time average drag coefficient of the RAE 2822 airfoil at Mach 0.78, while maintaining the average lift coefficient. We believe that this improvement may be attributed to the reduction of the shock strength. These results suggest that the application of shape optimization techniques could yield significant improvements in helicopter rotors or other unsteady devices operating in the transonic regime. Such optimizations might be prohibitively expensive for three dimensional applications with unsteady time domain methods. They might however, be enabled by the NLFD method, because it is both accurate enough and sufficiently efficient to make them computationally feasible.

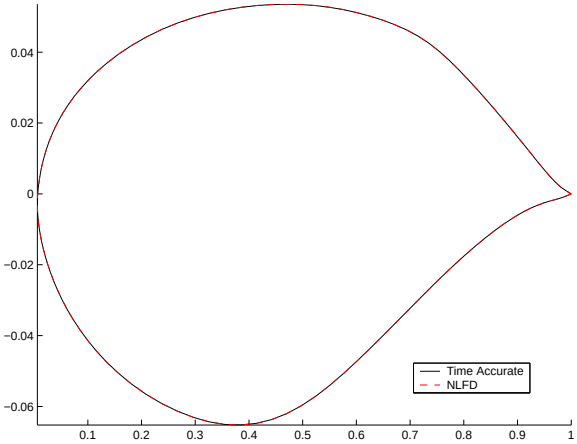

Fig. 14 Comparison of the Final Airfoil Geometry Between the Time Accurate and NLFD Method with Lift Constraints.

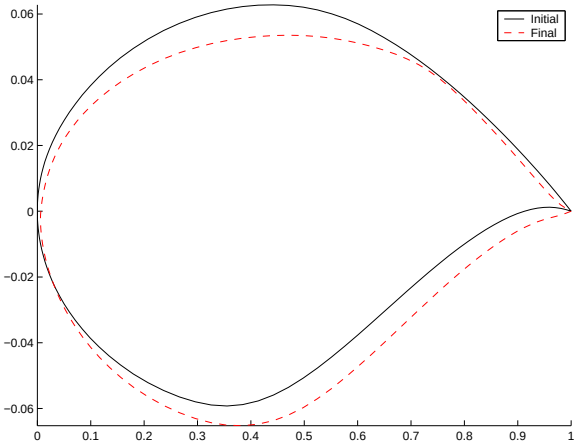

Fig. 15 Comparison of the Initial and Final Airfoil Geometry using the NLFD Method with Lift Constraints.

Acknowledgments

Some of the work accomplished in this research was conducted by Nadarajah while he was a graduate student at Stanford University. This research has ben-

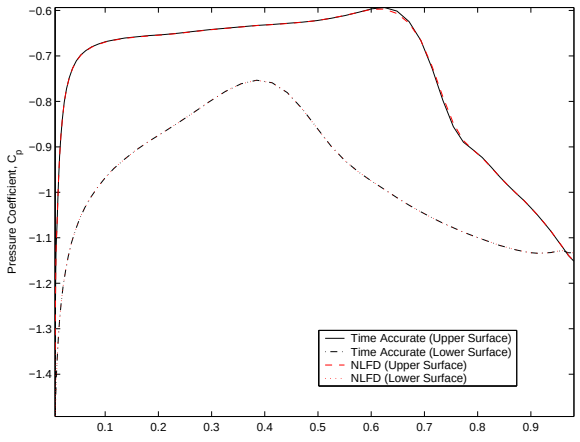

Fig. 16 Comparison of the Final Pressure Distribution Between the Time Accurate and NLFD Method with Lift Constraints.

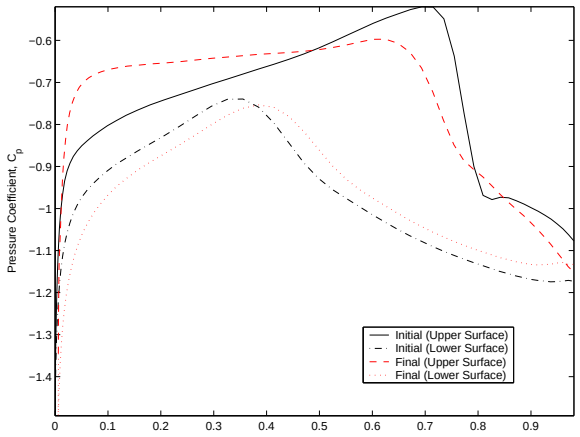

Fig. 17 Comparison of the Initial and Final Pressure Distribution using the NLFD method with Lift Constraints.

efited greatly from the generous support of the US AFOSR under grant number AF F49620-98-1-022, and the US Department of Energy under contract number LLNL B341491 as part of the Accelerated Strategic Computing Initiative program.

References

[1]J. J. Adamczyk. Model equation for simulating flows in multistage turbomachinery. Technical report, NASA Technical Memorandum 86869., Nov 1984.

[2]W. K. Anderson and V. Venkatakrishnan. Aerodynamic design optimization on unstructured grids with a continuous adjoint formulation. *AIAA paper 97-0643*, 35th Aerospace Sciences Meeting and Exhibit, Reno, Nevada, January 1997.

[3]R. Davis. Personal Communications on TFLO, January-December 2001.

[4]S. S. Davis. NACA 64A010 (NASA Ames model) oscillatory pitching. AGARD Report 702, August 1982. In Compendium of Unsteady Aerodynamic Measurements.

[5]M. C. Duta, M. .B. Giles, and M. S. Campobasso. The harmonic adjoint approach to unsteady turbomachinery design. *International Journal for Numerical Methods in Fluids*, 40:323–332, October 2002.

[6]J. Elliot and J. Peraire. Aerodynamic design using unstructured meshes. *AIAA paper 96-1941*, 1996.

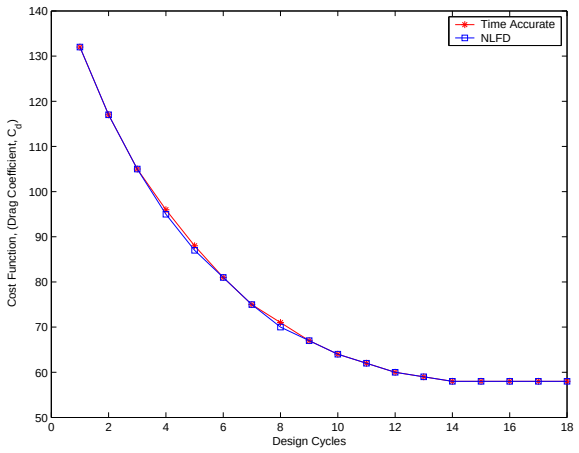

Fig. 18 Comparison of the Convergence of the Cost Function for the Time Accurate and NLFD methods with Lift Constraints.

[7]K. C. Hall. Seminar on harmonic balance techniques. Technical report, Presented to the Aerospace Computing Lab, Stanford University, 2000.

[8]K. C. Hall, J. P. Thomas, and W. S. Clark. Computation of unsteady nonlinear flows in cascades using a harmonic balance technique. Technical report, 9th International Symposium on Unsteady Aerodynamics, Aeroacoustics and Aeroelasticity of Turbomachines, Lyon, France, September 2000.

[9]A. Jameson. Computational aerodynamics for aircraft design. *Science*, 245:361–371, 1989.

[10]A. Jameson. Time dependent calculations using multigrid, with applications to unsteady flows past airfoils and wings. *AIAA paper 91-1596*, AIAA 10th Computational Fluid Dynamics Conference, Honolulu, Hawaii, June 1991.

[11]A. Jameson. Optimum aerodynamic design using CFD and control theory. *AIAA paper 95-1729*, AIAA 12th Computational Fluid Dynamics Conference, San Diego, CA, June 1995.

[12]A. Jameson, W. Schmidt, and E. Turkel. Numerical solutions of the Euler equations by finite volume methods with Runge-Kutta time stepping schemes. *AIAA paper 81-1259*, January 1981.

[13]A. Jameson and J. C. Vassberg. Studies of alternative numerical optimization methods applied to the brachistochrone problem. *OptiCON 99*, 1999.

[14]M. McMullen, A. Jameson, and J. Alonso. Acceleration of convergence to a periodic steady state in turbomachinery flows. *AIAA paper 01-0152*, 39th. Aerospace Sciences Meething and Exhibit, Reno, NV, Jan 2001.

[15]M. McMullen, A. Jameson, and J. Alonso. Application of a non-linear frequency domain solver to the euler and navier-stokes equations. *AIAA paper 02-0120*, 40th. Aerospace Sciences Meething and Exhibit, Reno, NV, Jan 2002.

[16]Matthew McMullen. *The Application of Non-Linear Frequency Domain Methods to the Euler and Navier-Stokes Equations*. Ph.d. dissertation, Department of Aeronautics and Astronautics, Stanford University, Stanford, CA, March 2003.

[17]S. Nadarajah and A. Jameson. Optimal control of unsteady flows using a time accurate method. *AIAA paper 2002-5436*, 9th. AIAA/ISSMO Symposium on Multidisciplinary Analysis and Optimization Conference, Atlanta, GA, September 2002.

[18]S. Nadarajah, A. Jameson, and J. J. Alonso. Sonic boom reduction using an adjoint method for wing-body configurations in supersonic flow. *AIAA paper 2002-5547*, 9th. AIAA/ISSMO Symposium on Multidisciplinary Analysis and Optimization Conference, Atlanta, GA, September 2002.

[19]Siva Nadarajah. *The Discrete Adjoint Approach to Aerodynamic Shape Optimization*. Ph.d. dissertation, Department

of Aeronautics and Astronautics, Stanford University, Stanford, CA, January 2003.

[20] J. Reuther, J.J. Alonso, M.J. Rimlinger, and A. Jameson. Aerodynamic shape optimization of supersonic aircraft configurations via an adjoint formulation on parallel computers. *AIAA paper 96-4045*, 6th AIAA/NASA/ISSMO Symposium on Multidisciplinary Analysis and Optimization, Bellevue, WA, September 1996.

[21] J. Reuther, A. Jameson, J. Farmer, L. Martinelli, and D. Saunders. Aerodynamic shape optimization of complex aircraft configurations via an adjoint formulation. *AIAA paper 96-0094*, 34th Aerospace Sciences Meeting and Exhibit, Reno, Nevada, January 1996.

[22] A. Snider. An Improved Estimate of the Accuracy of Trigonometric Interpolation. *SIAM Journal on Numerical Analysis*, 9(3):505–508, 1972.

[23] J. P. Thomas, K. C. Hall, and E. H. Dowell. A discrete adjoint approach for modelling unsteady aerodynamic design sensitivities. *AIAA paper 03-0041*, 41th. Aerospace Sciences Meething and Exhibit, Reno, NV, Jan 2003.